Geophysical Research Letters

RESEARCH LETTER
10.1029/2024GL111281

# Severe Strain-Induced Olivine-Ringwoodite Transformation at Room Temperature: Key to Enigmas of Deep-Focus Earthquake

**F. Lin[1], V. I. Levitas[1,2,3], S. Yesudhas[1], A. Dhar[1], and J. Smith[4]**

[1]Department of Aerospace Engineering, Iowa State University, Ames, IA, USA, [2]Department of Mechanical Engineering, Iowa State University, Ames, IA, USA, [3]Ames National Laboratory, US Department of Energy, Iowa State University, Ames, IA, USA, [4]X-ray Science Division, HPCAT, Argonne National Laboratory, Argonne, IL, USA

**Key Points:**

- Olivine-ringwoodite phase transformation (PT) is achieved at room temperature for the first time
- Minimum PT pressure decreases with the increasing plastic strain
- Strain-induced PT mechanism is the key to explaining the existing enigmas of deep-focus earthquakes

**Supporting Information:**

Supporting Information may be found in the online version of this article.

**Correspondence to:**

F. Lin and V. I. Levitas,
flin1@iastate.edu;
vlevitas@iastate.edu

**Citation:**

Lin, F., Levitas, V. I., Yesudhas, S., Dhar, A., & Smith, J. (2025). Severe strain-induced olivine-ringwoodite transformation at room temperature: Key to enigmas of deep-focus earthquake. *Geophysical Research Letters*, *52*, e2024GL111281. https://doi.org/10.1029/2024GL111281

Received 12 JUL 2024
Accepted 9 FEB 2025

**Author Contributions:**

**Conceptualization:** F. Lin, V. I. Levitas
**Formal analysis:** F. Lin, A. Dhar
**Funding acquisition:** V. I. Levitas
**Investigation:** F. Lin, S. Yesudhas, J. Smith
**Supervision:** V. I. Levitas
**Writing – original draft:** F. Lin, V. I. Levitas
**Writing – review & editing:** F. Lin, V. I. Levitas



**Abstract** Deep-focus earthquakes at 350–660 km are presumably caused by olivine-spinel phase transformation (PT). This cannot, however, explain the observed high seismic strain rate, which requires PT to complete within seconds, while metastable olivine does not transform for over a million years. Recent theory quantitatively describes how severe plastic deformations (SPD) can solve this dilemma but lacking experimental proof. Here, we introduce dynamic rotational diamond anvil cell with rough diamond anvils to impose SPD on San Carlos olivine. While olivine never transformed to spinel at room temperature, we obtained reversible olivine-ringwoodite PT under SPD at 15–28 GPa within tens of seconds. The PT pressure reduces with increasing dislocation density, microstrain, plastic strain, and decreasing crystallite size. Results demonstrate a new strain-induced PT mechanism compared to a pressure/temperature-induced one. Combined with SPD during olivine subduction, this mechanism can accelerate olivine-ringwoodite PT from millions of years to timescales relevant to earthquakes.

**Plain Language Summary** The mechanisms of deep-focus earthquakes remain a puzzle for decades. Although it is believed to be caused by olivine-spinel phase transformation (PT), it does not deliver answers to many enigmas, including the most important one: how does the PT occur so fast to produce high seismic strain rate (10–$10^3$/s) while olivine does not transform in metastable region for millions years. In previous studies, the PT of olivine was obtained under high pressure and temperature, which is treated as a stress/temperature-induced one. For the first time, we successfully induced PT by severe plastic deformation within tens of seconds at room temperature, which is clearly attributed to the effect of plastic strain. Hereby, this is a strain-induced transformation mechanism, distinguished from a pressure/temperature-induced one. The rate of strain-induced PT is proportional to the plastic strain rate (in addition to the pressure overshoot), and a high strain rate leads to a high transformation rate. In the Earth's interior, strain-induced PT and transformation-induced plastic strain promote each other, leading to continuous heating and further drastic increase of strain rate and PT rate required to trigger deep-focus earthquake in the subducted slabs.

## 1. Introduction

Deep-focus earthquakes (DFE) occur at 350–600 km within pressures of 12–23 GPa and 900–2000 K and cannot be explained by brittle fracture, in contrast to shallow earthquakes (Frohlich, 1989). The main hypothesis is that the DFE are caused by shear localization due to phase transformation (PT) of the subducted metastable olivine to denser wadsleyite or ringwoodite (Gasc, Daigre, et al., 2022; Gasc, Gardonio, et al., 2022; Green & Burnley, 1989; Green et al., 2015; Kirby, 1987; Kirby et al., 1996; Officer & Secco, 2020; Ohuchi et al., 2022; Schubnel et al., 2013; Wang et al., 2017; Wu et al., 1993; Zhan, 2020). However, one of the most disturbing among many existing enigmas is: How does metastable olivine, which does not completely transform to spinel deeply in the region of stability of spinel for over a million years, suddenly transform in shear bands within seconds to produce $10^{18}$ times jump from geological scale to seismic strain rates of 10–$10^3$/s? A new mechanism and quantitative theory in Levitas (2022) (see also Section S5 in Supporting Information S1) addresses this issue and also analyses alternative approaches from the abovementioned papers. The main point is that the olivine-spinel PT is treated as plastic strain-induced (instead of pressure/stress/temperature-induced), leading to entirely different thermodynamic and kinetic treatments. The fundamental difference between stress and strain-induced PT was formulated in Levitas (2004) and elaborated theoretically, computationally, and experimentally

in Javanbakht and Levitas (2016), Levitas (2019), Levitas (2023); Levitas and Javanbakht (2014), Lin et al. (2023b), Pandey and Levitas (2020), and Yesudhas et al. (2024). The key feature is that the strain-induced PT process is driven by accumulated plastic strain $q$, which substitutes time and serves as a time-like parameter. The kinetic equation for volume fraction $c$ of the ringwoodite is (Levitas, 2004):

$$\frac{dc}{dq} = k\,(1-c)\frac{\sigma_{yr}}{c\sigma_{yo}+(1-c)\sigma_{yr}}\left(p-p_{\varepsilon}^{d}\right) \rightarrow \frac{dc}{dt} = k\,(1-c)\frac{\sigma_{yr}}{c\sigma_{yo}+(1-c)\sigma_{yr}}\left(p-p_{\varepsilon}^{d}\right)\frac{dq}{dt} \text{ for } p > p_{\varepsilon}^{d}(q). \quad (1)$$

Here, $p_{\varepsilon}^{d}$ is the minimum pressure for initiating the plastic strain-induced PT, $\sigma_{yo}$ and $\sigma_{yr}$ are the yield strength of olivine and ringwoodite, respectively, and $k$ is the kinetic coefficient. PT starts when pressure $p$ exceeds the minimum pressure for strain-induced PT $p_{\varepsilon}^{d}$. Consequently, the PT rate is proportional to the plastic straining rate, and thus high strain rate leads to high PT rate. All parameters in Equation 1 depend on temperature. *However, there was no experimental proof of the existence of strain-induced PT for olivine or any geological material.* This study introduces dynamic rotational diamond anvil cell (dRDAC) with rough diamond anvils to severely deform San Carlos olivine. We conceptually prove that severe plastic deformation (SPD), even at room temperature, can induce the olivine-spinel PT within tens of seconds in the range of pressure 15–28 GPa, plastic strain 2.3–9, and strain rate $3.5 \times 10^{-3}$–$3.3 \times 10^{-2}$/s. Olivine transforms directly to ringwoodite without involving wadsleyite. The decreasing minimum PT pressure with increasing plastic strain and stagnation of PT evolution without plastic straining are consistent with the features of the strain-induced PT mechanism. During pressure release, ringwoodite completely transforms back to olivine at 2 GPa, which potentially affects the interpretation of some results of ex-situ studies. Finite element analysis (FEA) of the sample behavior in the dRDAC reproduces some important experimental observations and implies that the shear-PT bands in the sample are developed, which is required for our DFE theory (Levitas, 2022). Obtained results show that SPD and strain-induced PT of olivine is the key to comprehending the mechanism of DFE. In addition to the main results related to DFE, we determined the rules of the evolution of the microstructural parameters under high-pressure SPD with in-situ measurements.

## 2. Experimental Details and Methods

To impose high-pressure SPD, dRDAC is introduced, which allows one to produce the rotation of the piston anvil with a controllable rate in broad ranges (Figures 1a and 1b). To successfully induce PT with maximally reduced PT pressure, the maximized plastic strain is needed. This follows from our previous experience with Zr (Lin et al., 2023b; Pandey & Levitas, 2020) and Si (Yesudhas et al., 2024), and theoretical predictions (Levitas, 2004). Due to relative sliding between the sample and standard anvils, the rotation of the sample may be just 1/5 of the anvil (Pandey & Levitas, 2021). Thus, the rough diamond anvils with the periodic asperity height of 300 nm (10 nm for standard anvils) are implemented in the dRDAC (Figure 1c). Asperities penetrate the sample surface and eliminate the sliding. Sliding is substituted with a thin shear band near the contact surface, in which shear stress reaches the yield strength in shear. This promotes plastic flow and PT. The natural San Carlos olivine $(Mg_{0.91}Fe_{0.09})_2SiO_4$ is used with detailed compositions shown in Table S1 in Supporting Information S1. Ground powder sample is loaded in an iron gasket with an indented thickness of 150 μm and a sample chamber diameter of 200 μm. The sample is compressed and sheared using the dRDAC, following the deformation path defined in Table S2 in Supporting Information S1. Compressions are imposed with a gas-membrane system, and shears are imposed with a servomotor within dRDAC at a controllable rotation rate. Rotation rates of 1 and 0.1 rotation/min are imposed before (without PT) and after reaching 180° rotation, respectively. After each shear step, diffraction images were taken along the sample radius with a wavelength of 0.3445 Å and 10 μm step size. Sample thickness (Table S2 in Supporting Information S1) is measured through X-ray absorption of the indented gasket area using a linear attenuation equation. All measurements were performed at 16-ID-B beamline at HPCAT at Advanced Photon Source (APS) and recorded with the Pilatus detector. The instrument broadening was calibrated using a $CeO_2$ standard. The diffraction images were converted to unrolled patterns using FIT2D (Hammersley, 1997) and then analyzed through Rietveld refinement using MAUD software (Lutterotti et al., 1997) to obtain volume fraction of ringwoodite $\overline{c}$, crystallite sizes $d$, microstrains $\epsilon_m$, and lattice parameters, averaged over the sample thickness. The pressure was calibrated using third Birch-Murnaghan equation of state of San Carlos olivine from Liu et al. (2005). The dislocation density $\rho$ of olivine is estimated using Williamson-Hall method (Williamson & Smallman, 1956) with the easiest slip system (010)[001] from Raterron et al. (2014) (see Supporting Information S1). The radial distributions of the pressure, volume fraction of ringwoodite, dislocation density, microstrain,

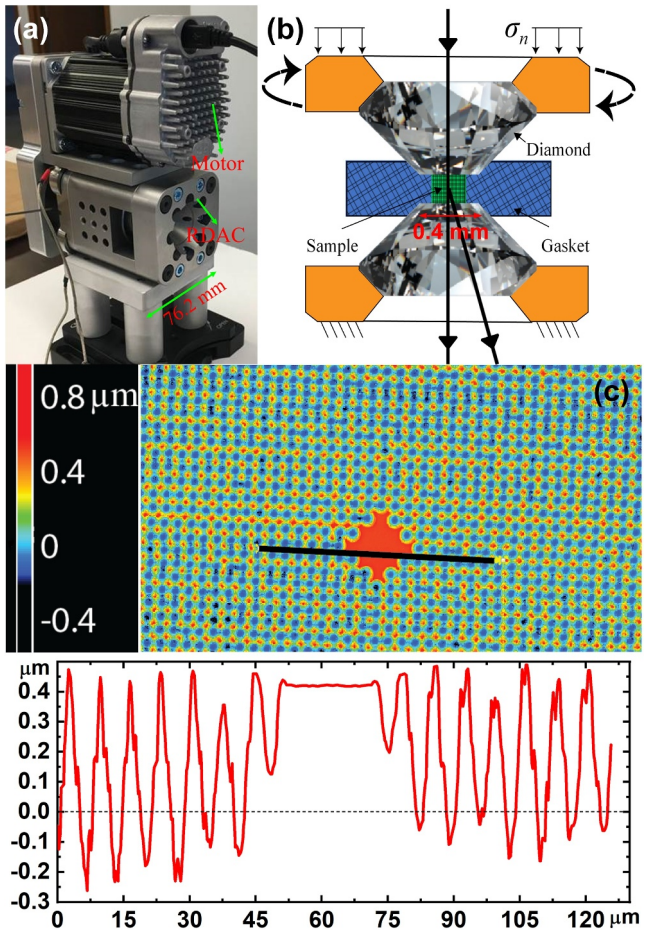


**Figure 1.** Dynamic rotational diamond anvil cell (dRDAC) with rough diamond anvils. (a) Design of dRDAC (DAC Tools LCC, Dr. Stanislav Sinogeikin); (b) Schematic of dRDAC; (c) Periodic asperity profiles at the surface of diamond anvil produced by laser ablation (PALM-Scientific LLC, Dr. Sergey Antipov). The sinusoidal curve is the measured relative asperities height along the black line.

and crystallite size, all averaged over the sample thickness, were determined for different fixed forces and rotation angles.

## 3. Results

Compression-shear steps in the experiment and the corresponding sample thickness $h$ are shown in Table S2 in Supporting Information S1. Compression from $h$ = 149–104 μm followed by 60° rotation (leading to $h$ = 75 μm), compression to $h$ = 73 μm, rotation by additional 120° to $\phi$ = 180° ($h$ = 53 μm), and compression to $h$ = 48 μm did not lead to PT. Figures 2a and 2b show an example of XRD diffraction patterns without PT at rotation angle $\phi$ = 180°. Pressure is in the range of 6–8 GPa (Figure 3a), which is deeply in the stability field of the olivine, and no PT is found. After imposing compression and another 90° rotation to $\phi$ = 270° (Figures 2c and 2d), pressure increases significantly with a radial pressure gradient (Figure 3a). Ringwoodite phase was first time observed at $\phi$ = 270° with the maximum $\bar{c}$ = 0.4 at the sample center and decreasing down to zero toward the edge (Figure 3b). With further rotation to 300° and 330°, the pressure distribution is stabilized and does not change essentially. Although it is not feasible to experimentally track the deformation path of each material particle within the sample, plastic strain $q$ at the current thickness $h$ and radius $r$ with respect to the culet center can be approximately estimated as (Edalati et al., 2022):

$$q = ln\left(\frac{h}{h_0}\right) + \frac{\phi r}{\sqrt{3}h} \quad (2)$$

with $h_0$ being the initial thickness of the sample. Since shear strains are imposed at different $h$, Equation 2 is used incrementally between each step along the deformation path and combining all increments.

To reveal the main rules of the microstructure evolution and its relation to plastic strain and strain-induced PT, we track in situ the evolution of the radial distribution of the crystallite size $d$, microstrain $\varepsilon_m$, and dislocation density $\rho$ averaged over the sample thickness (Figures 3c–3e). At $\phi$ = 180°, $d$, $\rho$, and $\varepsilon_m$ are around 40–60 nm, 2.5 × $10^{14}$ $m^{-2}$, and 0.008–0.010, respectively. At $\phi$ = 270° with PT first time being observed, $d$ of olivine significantly decreases to ~25 nm, and $\rho$ and $\varepsilon_m$ increase to ~5.5 × $10^{14}$ $m^{-2}$ and ~0.01, respectively. The following two rotation increments do not essentially change the radial distribution of $d$ and $\varepsilon_m$ in olivine (Figures 3d and 3e). Considering statistical scatter and including all data for $\phi$ = 270°–330° and all radii, we may conclude that crystallite size and microstrain of olivine are homogenous and steady. However, the pressure, plastic strain, strain path (compression-shear), and volume fraction of the ringwoodite $\bar{c}$ varies substantially along the radius and for different rotations. Thus, the obtained results imply a new informative rule of coupled SPD, strain-induced PT, and microstructure evolution: after high-pressure SPD, an averaged crystallite size and microstrain of the olivine during PT is getting steady and independent of *plastic strain, strain path, pressure, and* $\bar{c}$, that is, *deformation path and completeness of PT*. At $\phi$ = 270° and 300°, $\rho$ is also practically constant along the radius with the same independence as $d$ and $\varepsilon_m$. However, at $\phi$ = 330°, scatter significantly increases, and no such conclusion can be made. Increasing heterogeneous processes due to shear strain and PT may cause this. The crystallite size of ringwoodite is small, around 5–10 nm (Figure 3d), and is steady and independent of the *deformation path and completeness of PT* as well.

The minimum PT pressure $p_\varepsilon^d$, as a key parameter of the PT kinetics, is found as a linearly decreasing function of $q$ in Figure 4a using only the data around the edge where PT starts ($\bar{c} < 0.1$). Since at these points, $d$ of olivine linearly reduces with increasing $q$, and $\rho$ and $\varepsilon_m$ linearly increase with increasing $q$ (see Equations S17–S19 in Supporting Information S1), the $p_\varepsilon^d$ can also be expressed as a linear function of the dislocation density, microstrain, and crystallite size (Figures 4b–4d).

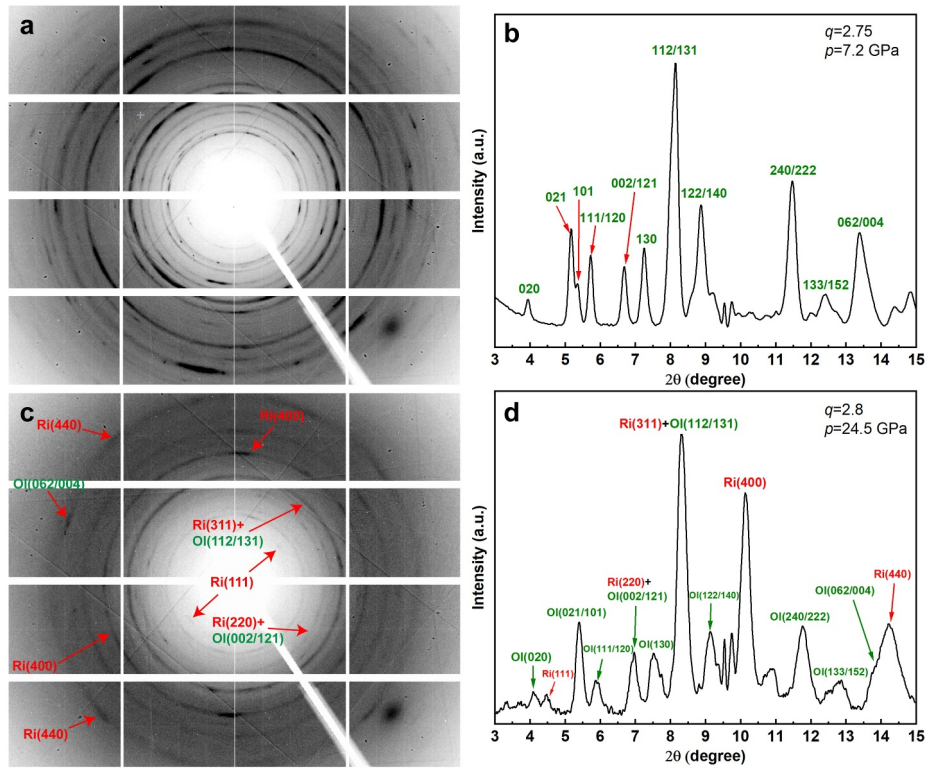


**Figure 2.** X-ray diffraction patterns of the deformed olivine sample. (a) 2D patterns and (b) integrated peak profiles after olivine reaching $p = 7.2$ GPa at the sample center and 180° of anvil rotation. No phase transformation (PT) was observed. (c) 2D patterns and (d) integrated peak profiles of olivine and ringwoodite after reaching $p = 24.5$ GPa at the sample center and 270° of anvil rotation.

During unloading, ringwoodite unexpectedly fully transforms back to olivine at 2 GPa. The sample was pulverized during complete anvil separation.

To reproduce the phase evolution process, we perform FEA of the deformation of the sample confined in a gasket with the dRDAC. While precise simulations are impossible due to the lack of some properties versus $\overline{c}$ and unknown PT kinetics (see Supporting Information S1), to prove the concept, we followed similar problem formulation like in Feng and Levitas (2016) and found a generic FEA solution for a material with the yield strength in shear $\tau_y$ of the high-pressure Phase 3.33 times lower than that of the low-pressure phase, since the $\tau_y$ of the nanograined ringwoodite is much lower than olivine (Mohiuddin et al., 2020). The solution shows intersecting shear-PT bands (Figure 3f), one localized at the contact surface and the others inclined to the symmetry axis. The calculated curves for $\overline{c}$ are plotted in Figure 3g. After some torsions, the PT almost completes in each band, and further evolution of $\overline{c}$ is limited.

## 4. Discussion

With imposed high-pressure SPD using dRDAC, olivine-ringwoodite PT was induced at room temperature for the first time. Most of the previous experimental confirmations of PT-based mechanisms of DFE were obtained for structural analogs of the olivine, $Mg_2GeO_4$ (Gasc, Daigre, et al., 2022, Gasc, Gardonio, et al., 2022; Green et al., 2015; Schubnel et al., 2013; Wang et al., 2017), or $Fe_2SiO_4$ (Officer & Secco, 2020), in which PT occurs at much lower pressures and temperatures. In this case, brittle fractures may occur first, and friction at the shear crack surfaces may cause PT (Gasc, Gardonio, et al., 2022) rather than vice versa. No PT was observed for $(Mg_{1-x}Fe_x)_2SiO_4$ for any Fe content at room temperature up to more than 50 GPa (Andrault et al., 1995), indicating that high pressure itself cannot induce PT. In experiments involving plastic deformation of olivine (Mohiuddin et al., 2020; Ohuchi et al., 2022), strain is relatively small (~0.3), and heating above 1100 K for hours is required for PT to occur; these PTs were treated as pressure/temperature-induced ones, that is, transformation

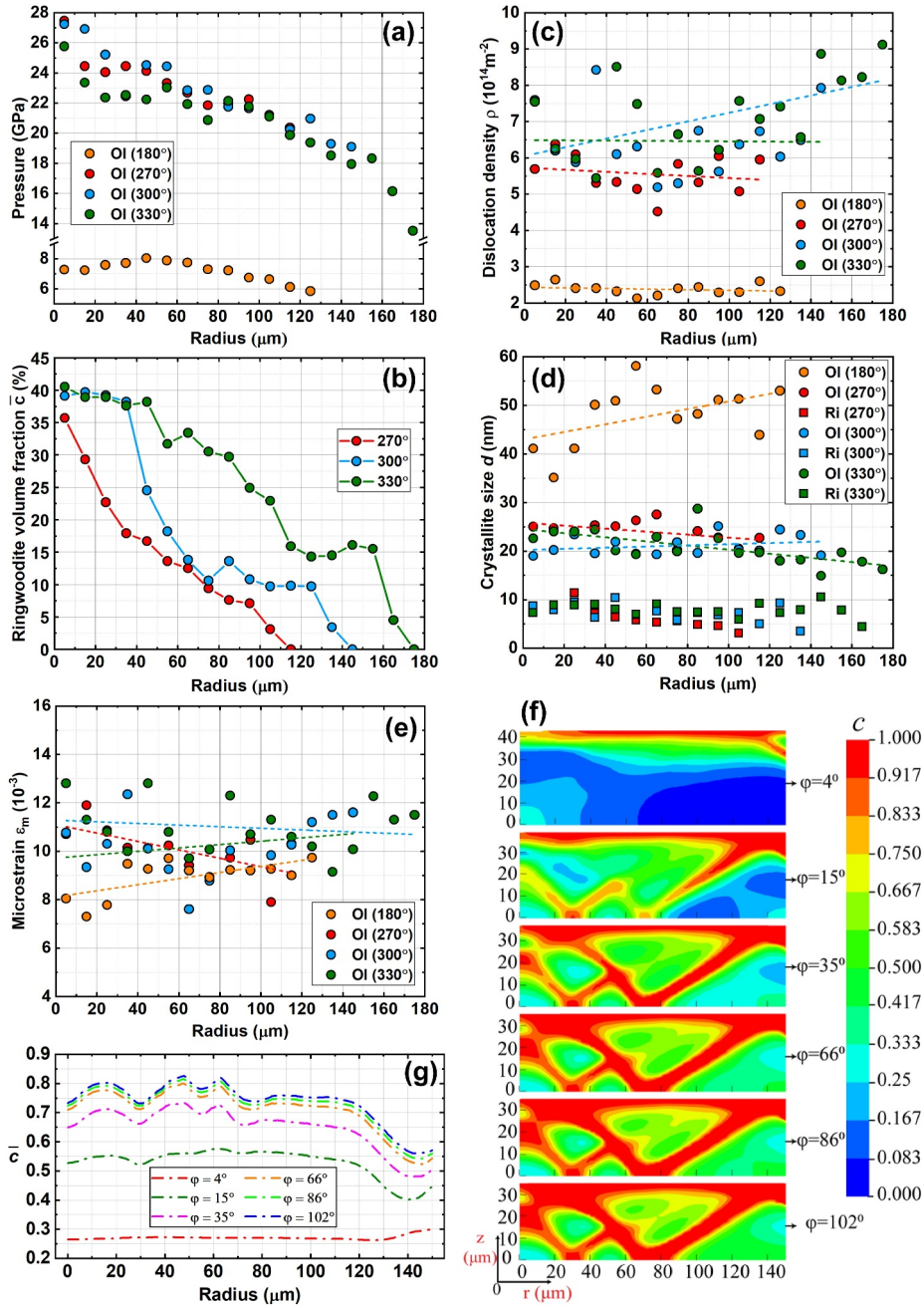


**Figure 3.** Radial distributions of various parameters in the samples after different compression-shear loadings in dRDAC. (a) Pressure, (b) volume fraction of the ringwoodite, (c) dislocation density, (d) crystallite size, and (e) microstrain. Results from the finite element analysis under a constant compressive force with increasing rotation angle $\phi$. (f) Radial distribution of the volume fraction of the weaker ringwoodite $c$ within the central part of the sample. (g) Radial distribution of the volume fraction of the ringwoodite $\bar{c}$ averaged over the sample thickness. The uncertainties of all parameters in figures (a)–(e) are smaller than the symbols.

kinetics was discussed/described in terms of pressure, temperature, and time without involving plastic strain. Thus, the PT in this study is clearly attributed to the SPD. It demonstrates that high temperature is not required for SPD-induced transformation to occur. This is opposite to the statements in Wu et al. (1993) and Ohuchi et al. (2022) that olivine-spinel transformation in subducting slab starts when a critical temperature is reached.

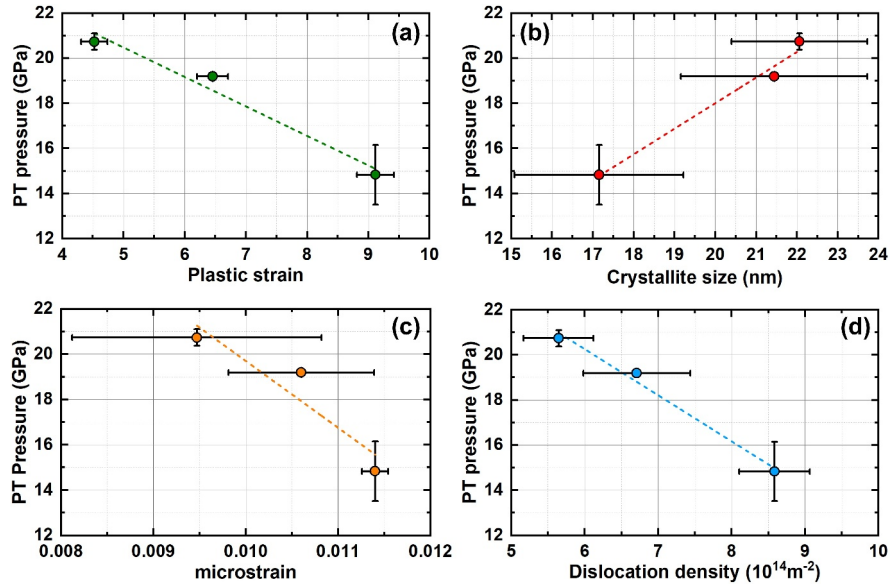


**Figure 4.** Minimum pressure for initiation of strain-induced PT $p_{\dot{\varepsilon}}^{d}$ versus (a) plastic strain, (b) crystallite size, (c) microstrain, and (d) dislocation density.

In addition, comparing the evolution of the ringwoodite $\overline{c}$ from $\phi = 270°$ to 330° rotation at the same radii in Figure 3b, where pressures are very close (Figure 3a), but shears and compressions strain increase with torsion, we see that the $\overline{c}$ increases with increasing $q$, which is consistent with the strain-controlled kinetic Equation 1. The $\overline{c}$ does not evolve after the rotation stops, that is, time is irrelevant for phase evolution, like in Equation 1. With a rotation rate of 0.1 RPM, 30° shear increment takes 50 s, which is a characteristic time for PT in this experiment. As it follows from Equation 1, increasing the rotation rate would reduce the characteristic PT time proportionally. Thus, utilizing strain-induced PT versus pressure/temperature-induced PT could reduce the PT time from millions of years to seconds, which is required for the PT-based mechanism of the DFE to produce a high seismic strain rate (Levitas, 2022). The minimum PT pressure $p_{\dot{\varepsilon}}^{d}$ reduces with plastic strain (Figure 4a), which is also a key feature of strain-induced PT, while for pressure-induced PTs, plastic straining usually increases the minimum PT pressure (Yesudhas et al., 2024). This explains the necessity of SPD for strain-induced olivine-ringwoodite PT, which is easily achieved in geodynamic activity but not in previous experiments. With a significant increase of the plastic strain, the PT pressure can potentially be further reduced below the current minimum value of 15 GPa (already slightly lower than the extrapolated phase equilibrium pressure between 15 and 16 GPa for wadsleyite-ringwoodite PT at 300 K (Ottonello et al., 2009)).

Since the strain-induced PT kinetics is conceptually proved, it is used in FEA for phase evolution under SPD in dRDAC to bring new insights to the mechanism of DFE. The main generic result is that when the yield strength of the high-pressure phase is much lower than that of the low-pressure phase (like for olivine-ringwoodite (Mohiuddin et al., 2020)), shear-PT bands are formed in the sample (Figure 3f). Such bands are the crucial part for the mechanism of DFE in Levitas (2022). FEA also reproduces the following experimental results, supporting the existence of the shear-PT bands. (a) The radial distribution of the high-pressure phase shows similar non-monotonous features as the experiment due to a change in the number of shear PT bands along the radius (Figures 3b and 3g). This contrasts with monotonous radial distribution for materials with stronger high-pressure phase without shear-banding, like in Zr (Lin et al., 2023b; Pandey & Levitas, 2020). (b) The high-pressure phase stops evolving after a certain rotation (Figure 3g), similar to the experimental observation of the same maximum $\overline{c} \approx 0.4$ from $\phi = 300°$ to 330° near the sample center (Figure 3b); this is because most of the plastic strain is localized in weak PT-shear bands and strain-induced PT does not essentially spread outside of PT-shear bands.

Since we found that strain-induced olivine-spinel transformation is reversible during pressure release, currently, FEA is the only way to prove the existence of the shear-transformation bands. This also potentially affects the interpretation of some results of scanning/transmission electron microscopy (SEM/TEM) imaging. Indeed, shear-

transformation bands may disappear during unloading, and observed faults/cracks in olivine without spinel may also be caused by the direct-reverse PT. Since pressure/temperature-induced ringwoodite can be quenched (Mohiuddin et al., 2020), the observed reversibility demonstrates further difference between pressure/temperature- and strain-induced transformations at room temperature. Reversibility is probably caused by a large density of defects accumulated during SPD and transformation at room temperature.

Similar strain-induced PT is also expected at temperatures of 900–1200 K, relevant to DFE. Indeed, in non-hydrostatic DAC experiments on $Mg_2SiO_4$ (Wu et al., 1993), the thin $\beta$-spinel film appeared at the diamond surface at 19–35 GPa after holding at 575°C for 10.5 hr. No PT was found in bulk, which indicates that this PT is induced by large plastic shears due to friction in the contact region. Even at 28–32 GPa and 650°C for 8 hr, only wadsleyite was observed in bulk without ringwoodite. Larger plastic straining, increasing $\rho$ and $\varepsilon_m$ and decreasing $d$, should reduce transformation time to seconds.

Independent of the main results directly related to DFE, we discuss microstructure evolution since it strongly affects deformational and transformational behavior. Constant $d$ and $\varepsilon_m$ of olivine and $d$ of ringwoodite at different radii and loadings while the pressure, plastic strain, and strain path were different, show that after SPD, these values are getting steady and independent of pressure, plastic strain, and strain path. The same was observed in situ and concluded for $\omega$-Zr (Lin et al., 2023a). Below the maximum $\overline{c}$ achieved, which is ~0.4 here, the volume fraction of ringwoodite does not affect $d$, $\rho$, and $\varepsilon_m$ of olivine either, similar to the case of $\alpha$-$\omega$ PT in Zr (Lin et al., 2023b) when volume fraction of $\omega$-Zr is below ~0.5. Increase of dislocation density and reduction of crystallite size with plastic deformation are well-known for various materials and are the goal of modern SPD technologies (Edalati et al., 2022). Steady crystallite size, dislocation density, and hardness, homogenously distributed along the sample radius (similar to Figures 3c and 3d), are broadly obtained after SPD and load release for various metals and ceramics (Edalati & Horita, 2010; Edalati et al., 2022; Pippan et al., 2010). Here, we extend this rule to minerals for the first time with in-situ measurement. However, the volume fraction of ringwoodite does not affect the crystallite size of high-pressure phase either, in contrast to $\alpha$-$\omega$ PT in Zr (Lin et al., 2023b), which is new and nontrivial. The crystallite size of the ringwoodite is ~5–10 nm (Figure 3d). These are reasonable numbers, since in Mohiuddin et al. (2020), the grain size for ringwoodite of 12–20 nm was reported after small plastic strain of 7% at 1,173 K.

Obtained results call for reconsidering the experiments required to study the PT-based mechanism of the DFE. The temperature should be low enough to avoid pressure/temperature-induced transformation, and SPD should be applied instead. Preliminary plastic deformation at normal or low pressure leading to significant grain refinement and increase in dislocation density may essentially reduce plastic strain required for transformation at high pressure, similar to the case with Zr (Lin et al., 2023a, 2023b).

## 5. Conclusions

In summary, with newly introduced dRDAC and rough diamond anvils that generate SPD and in-situ measurements of the main parameters along the sample radius, we induced olivine-ringwoodite PT at room temperature for the first time within tens of seconds and received a conceptual proof of the strain-induced PT character and mechanism for this PT. The decreasing minimum PT pressure with increasing plastic strain, stagnation of PT progress without plastic straining, and change in PT path (without involving wadsleyite) are consistent with the features of strain-induced PT mechanism. The observed complete reversibility of this transformation during pressure release demonstrates an additional difference between pressure/temperature- and strain-induced transformations at room temperature. The reversibility of transformation also potentially challenges some interpretations of SEM/TEM studies. FEA of the sample behavior in dRDAC implies that for the olivine-spinel PT system, due to much smaller yield strength of spinel, the shear-PT bands in the sample are developed, which are required for the formation of DFE (Levitas, 2022).

The main rules of the coupled SPD, PT, and microstructure evolution are also found: after high-pressure SPD, the crystallite sizes and microstrain of olivine and crystallite sizes of ringwoodite during PT are getting steady and independent of *plastic strain, strain path, pressure, and volume fraction of ringwoodite*. At the initiation of PT, the minimum PT pressure reduces with increasing dislocation density, microstrain, and $q$, and with reducing crystallite size. Also, the crystallite size reduces, and dislocation density and microstrain increase with increasing $q$. Thus, the key to successfully reducing the minimum PT pressure was to increase $\rho$ and $\varepsilon_m$, and reduce $d$ by

SPD, which can be provided in the dRDAC or at the boundary of the subducting olivine wedge, especially within shear bands.

Our results confirm some of the main hypotheses of the mechanism of the DFE suggested in Levitas (2022): plastic strain-induced olivine-spinel transformation can occur and lead to shear-transformation bands in the pressure range and time scale relevant to conditions in the transition zone (even at much lower temperature), which was the main goal of the paper. They call for change in the main governing parameters (SPD instead of time) in discussions, modeling, and experimental studies of olivine-spinel transformation in relation to the DFE. They also open new directions for coupled experimental/theoretical/computational studies of strain-induced olivine-ringwoodite PT and shear localization in a broad range of strain rates and temperatures to qualitatively advance simulations of the DFE problems and larger-scale geodynamic processes during olivine slab subduction (Billen, 2020; Kawakatsu & Yoshioka, 2011). Obtained results also lead to reconsidering numerous known PTs in the Earth's interior as strain-induced instead of pressure/temperature-induced, which may change many geological interpretations. For example, they may explain the appearance of microdiamonds directly in the cold Earth crust within shear bands (Gao et al., 2019) without subduction to the high-pressure, high-temperature mantle and uplifting.

## Data Availability Statement

The synchrotron diffraction images used in this study are available at the Open Data Repository of Iowa State University (DataShare) via (Lin & Levitas, 2023) with Creative Commons Attribution (CC-BY) 4.0 International License.

**Acknowledgments**
Support from NSF (CMMI-1943710, DMR-2246991, and MSS170015), ARO (W911NF2420145), and Iowa State University (Vance Coffman Faculty Chair Professorship and Murray Harpole Chair in Engineering) is greatly appreciated. This work is performed at HPCAT (Sector 16), APS, and Argonne National Laboratory. HPCAT operations are supported by DOE-NNSA's Office of Experimental Science. The APS is a U.S. Department of Energy (DOE) Office of Science User Facility operated for the DOE Office of Science by Argonne National Laboratory under Contract No. DE-AC02-06CH11357. We thank Dr. K.K. Pandey (Bhabha Atomic Research Center, Mumbai, India) for developing RDAC techniques and measurements during his work as a postdoc at Iowa State University and for his help with the determination of microstructural parameters.

## References

Andrault, D., Bouhifd, M. A., Itie, J. P., & Richet, P. (1995). Compression and amorphization of $(Mg, Fe)_2SiO_4$ olivines: An X-ray diffraction study up to 70 GPa. *Physics and Chemistry of Minerals*, *22*(2), 99–107. https://doi.org/10.1007/bf00202469

Billen, M. I. (2020). Deep slab seismicity limited by rate of deformation in the transition zone. *Science Advances*, *6*(22), eaaz7692. https://doi.org/10.1126/sciadv.aaz7692

Edalati, K., Bachmaier, A., Beloshenko, V. A., Beygelzimer, Y., Blank, V. D., Botta, W. J., et al. (2022). Nanomaterials by severe plastic deformation: Review of historical developments and recent advances. *Materials Research Letters*, *10*(4), 163–256. https://doi.org/10.1080/21663831.2022.2029779

Edalati, K., & Horita, Z. (2010). Universal plot for hardness variation in pure metals processed by high-pressure torsion. *Materials Transactions*, *51*(5), 1051–1054. https://doi.org/10.2320/matertrans.m2009431

Feng, B., & Levitas, V. I. (2016). Effects of gasket on coupled plastic flow and strain-induced phase transformations under high pressure and large torsion in a rotational diamond anvil cell. *Journal of Applied Physics*, *119*(1), 015902. https://doi.org/10.1063/1.4939488

Frohlich, C. (1989). The nature of deep-focus earthquakes. *Annual Review of Earth and Planetary Sciences*, *17*(1), 227–254. https://doi.org/10.1146/annurev.ea.17.050189.001303

Gao, Y., Ma, Y., An, Q., Levitas, V., Zhang, Y., Feng, B., et al. (2019). Shear driven formation of nano-diamonds at sub-gigapascals and 300 K. *Carbon*, *146*, 364–368. https://doi.org/10.1016/j.carbon.2019.02.012

Gasc, J., Daigre, C., Moarefvand, A., Deldicque, D., Fauconnier, J., Gardonio, B., et al. (2022). Deep-focus earthquakes: From high-temperature experiments to cold slab. *Geology*, *50*(9), 1018–1022. https://doi.org/10.1130/g50084.1

Gasc, J., Gardonio, B., Deldicque, D., Daigre, C., Moarefvand, A., Petit, L., et al. (2022). Ductile vs. Brittle strain localization induced by the olivine–ringwoodite transformation. *Minerals*, *12*(6), 719. https://doi.org/10.3390/min12060719

Green, H. W., & Burnley, P. C. (1989). A new, self-organizing, mechanism for deep-focus earthquakes. *Nature*, *341*, 733–737.

Green, II, H. W., Shi, F., Bozhilov, K., Xia, G., & Reches, Z. (2015). Phase transformation and nanometric flow cause extreme weakening during fault slip. *Nature Geoscience*, *8*(6), 484–489. https://doi.org/10.1038/ngeo2436

Hammersley, A. P. (1997). FIT2D: An introduction and overview, *European Synchrotron Radiation Facility Internal Report ESRF97HA02T* (Vol. *68*, p. 58).

Javanbakht, M., & Levitas, V. I. (2016). Phase field simulations of plastic strain-induced phase transformations under high pressure and large shear. *Physical Review B*, *94*(21), 214104. https://doi.org/10.1103/physrevb.94.214104

Kawakatsu, H., & Yoshioka, S. (2011). Metastable olivine wedge and deep dry cold slab beneath southwest Japan. *Earth and Planetary Science Letters*, *303*(1–2), 1–10. https://doi.org/10.1016/j.epsl.2011.01.008

Kirby, S. H. (1987). Localized polymorphic phase transformations in high-pressure faults and applications to the physical mechanism of deep earthquakes. *Journal of Geophysical Research: Solid Earth*, *92*(B13), 13789–13800. https://doi.org/10.1029/jb092ib13p13789

Kirby, S. H., Stein, S., Okal, E. A., & Rubie, D. C. (1996). Metastable mantle phase transformations and deep earthquakes in subducting oceanic lithosphere. *Reviews of Geophysics*, *34*(2), 261–306. https://doi.org/10.1029/96rg01050

Levitas, V. I. (2004). High-pressure mechanochemistry: Conceptual multiscale theory and interpretation of experiments. *Physical Review B*, *70*(18), 184118. https://doi.org/10.1103/physrevb.70.184118

Levitas, V. I. (2019). High-pressure phase transformations under severe plastic deformation by torsion in rotational anvils. *Materials Transactions*, *60*(7), 1294–1301. https://doi.org/10.2320/matertrans.mf201923

Levitas, V. I. (2022). Resolving puzzles of the phase-transformation-based mechanism of the deep-focus earthquake. *Nature Communications*, *13*(1), 6291. https://doi.org/10.1038/s41467-022-33802-y

Levitas, V. I. (2023). Recent in situ experimental and theoretical advances in severe plastic deformations, strain-induced phase transformations, and microstructure evolution under high pressure. *Materials Transactions*, *64*(8), 1866–1878. https://doi.org/10.2320/matertrans.mt-mf2022055

Levitas, V. I., & Javanbakht, M. (2014). Phase transformations in nanograin materials under high pressure and plastic shear: Nanoscale mechanisms. *Nanoscale*, *6*(1), 162–166. https://doi.org/10.1039/c3nr05044k

Lin, F., & Levitas, V. (2023). Synchrotron diffraction images of san Carlos olivine deformed in a rotational diamond anvil cell [Dataset]. *Iowa State University*. https://doi.org/10.25380/iastate.24839280.v1

Lin, F., Levitas, V. I., Pandey, K. K., Yesudhas, S., & Park, C. (2023a). In-situ study of rules of nanostructure evolution, severe plastic deformations, and friction under high pressure. *Materials Research Letters*, *11*(9), 757–763. https://doi.org/10.1080/21663831.2023.2231983

Lin, F., Levitas, V. I., Pandey, K. K., Yesudhas, S., & Park, C. (2023b). Rules of plastic strain-induced phase transformations and nanostructure evolution under high-pressure and severe plastic flow. *May*, *23*, 23. https://doi.org/10.48550/arXiv.2305.15737

Liu, W., Kung, J., & Li, B. (2005). Elasticity of San Carlos olivine to 8 GPa and 1073 K. *Geophysical Research Letters*, *32*(16), L16301. https://doi.org/10.1029/2005gl023453

Lutterotti, L., Matthies, S., Wenk, H. R., Schultz, A. S., & Richardson, J. W., Jr. (1997). Combined texture and structure analysis of deformed limestone from time-of-flight neutron diffraction spectra. *Journal of Applied Physics*, *81*(2), 594–600. https://doi.org/10.1063/1.364220

Mohiuddin, A., Karato, S.-I., & Girard, J. (2020). Slab weakening during the olivine to ringwoodite transition in the mantle. *Nature Geoscience*, *13*(2), 170–174. https://doi.org/10.1038/s41561-019-0523-3

Officer, T., & Secco, R. A. (2020). Detection of high P,T transformational faulting in Fe2SiO4 via in-situ acoustic emission: Relevance to deep-focus earthquakes. *Physics of the Earth and Planetary Interiors*, *300*, 106429. https://doi.org/10.1016/j.pepi.2020.106429

Ohuchi, T., Higo, Y., Tange, Y., Sakai, T., Matsuda, K., & Irifune, T. (2022). In situ X-ray and acoustic observations of deep seismic faulting upon phase transitions in olivine. *Nature Communications*, *13*(1), 5213. https://doi.org/10.1038/s41467-022-32923-8

Ottonello, G., Civalleri, B., Ganguly, J., Zuccolini, M. V., & Noel, Y. (2009). Thermophysical properties of the $\alpha$–$\beta$–$\gamma$ polymorphs of Mg2SiO4: A computational study. *Physics and Chemistry of Minerals*, *36*(2), 87–106. https://doi.org/10.1007/s00269-008-0260-4

Pandey, K. K., & Levitas, V. I. (2020). In situ quantitative study of plastic strain-induced phase transformations under high pressure: Example for ultra-pure Zr. *Acta Materialia*, *196*, 338–346. https://doi.org/10.1016/j.actamat.2020.06.015

Pandey, K. K., & Levitas, V. I. (2021). Displacement field measurements in traditional and rotational diamond anvil cells. *Journal of Applied Physics*, *129*(11), 115901. https://doi.org/10.1063/5.0044030

Pippan, R., Scheriau, S., Taylor, A., Hafok, M., Hohenwarter, A., & Bachmaier, A. (2010). Saturation of fragmentation during severe plastic deformation. *Annual Review of Materials Research*, *40*(1), 319–343. https://doi.org/10.1146/annurev-matsci-070909-104445

Raterron, P., Detrez, F., Castelnau, O., Bollinger, C., Cordier, P., & Merkel, S. (2014). Multiscale modeling of upper mantle plasticity: From single-crystal rheology to multiphase aggregate deformation. *Physics of the Earth and Planetary Interiors*, *228*, 232–243. https://doi.org/10.1016/j.pepi.2013.11.012

Schubnel, A., Brunet, F., Hilairet, N., Gasc, J., Wang, Y., & Green, H. W. (2013). Deep focus earthquake analogs recorded at high pressure and temperature in the laboratory. *Science*, *341*(6152), 1377–1380. https://doi.org/10.1126/science.1240206

Wang, Y., Zhu, L., Shi, F., Schubnel, A., Hilairet, N., Yu, T., et al. (2017). A laboratory nanoseismological study on deep-focus earthquake micromechanics. *Science Advances*, *3*(7), e1601896. https://doi.org/10.1126/sciadv.1601896

Williamson, G. K., & Smallman, III, R. E. (1956). Dislocation densities in some annealed and cold-worked metals from measurements on the X-ray Debye-Scherrer spectrum. *Philosophical Magazine*, *1*, 34–46. https://doi.org/10.1080/14786435608238074

Wu, T. C., Bassett, W. A., Burnley, P. C., & Weathers, M. S. (1993). Shear-promoted phase transitions in $Fe_2SiO_4$ and $Mg_2SiO_4$ and the mechanism of deep earthquakes. *Journal of Geophysical Research*, *98*(B11), 19767–19776. https://doi.org/10.1029/93jb01614

Yesudhas, S., Levitas, V. I., Lin, F., Pandey, K. K., & Smith, J. (2024). Unexpected plastic strain-induced phase transformation phenomena in silicon. *Nature Communications*, *15*(1), 7054. https://doi.org/10.1038/s41467-024-51469-5

Zhan, Z. (2020). Mechanisms and implications of deep earthquakes. *Annual Review of Earth and Planetary Sciences*, *48*(1), 147–174. https://doi.org/10.1146/annurev-earth-053018-060314

## References From the Supporting Information

Anderson, P. M., Hirth, J. P., & Lothe, J. (2017). *Theory of dislocations*. Cambridge University Press.

Borbély, A., & Ungár, T. (2012). X-ray line profiles analysis of plastically deformed metals. *Comptes Rendus Physique*, *13*(3), 293–306. https://doi.org/10.1016/j.crhy.2011.12.004

Chen, H., Levitas, V. I., & Xiong, L. (2019). Amorphization induced by 60° shuffle dislocation pileup against different grain boundaries in silicon bicrystal under shear. *Acta Materialia*, *179*, 287–295. https://doi.org/10.1016/j.actamat.2019.08.023

Dhar, A., Levitas, V. I., Pandey, K. K., Park, C., Somayazulu, M., & Velisavljevic, N. (2024). Quantitative kinetic rules for plastic strain-induced $\alpha$-$\omega$ phase transformation in Zr under high pressure. *Npj Computational Materials*, *10*, 290. https://doi.org/10.1038/s41524-024-01491-4

Edalati, K., Miresmaeili, R., Horita, Z., Kanayama, H., & Pippan, R. (2011). Significance of temperature increase in processing by high-pressure torsion. *Materials Science and Engineering A*, *528*(24), 7301–7305. https://doi.org/10.1016/j.msea.2011.06.031

Ji, C., Levitas, V. I., Zhu, H., Chaudhuri, J., Marathe, A., & Ma, Y. (2012). Shear-induced phase transition of nanocrystalline Hexagonal Boron Nitride to wurtzitic structure at room temperature and low pressure. *Proceedings of the National Academy of Sciences of the USA*, *109*(47), 19108–19112. https://doi.org/10.1073/pnas.1214976109

Lee, D. J., Yoon, E. Y., Ahn, D. H., Park, B. H., Park, H. W., Park, L. J., et al. (2014). Dislocation density-based finite element analysis of large strain deformation behavior of copper under high-pressure torsion. *Acta Materialia*, *76*, 281–293. https://doi.org/10.1016/j.actamat.2014.05.027

Levitas, V. I., Dhar, A., & Pandey, K. K. (2023). Tensorial stress-plastic strain fields in alpha-omega Zr mixture, transformation kinetics, and friction in diamond anvil cell. *Nature Communications*, *14*(1), 5955. https://doi.org/10.1038/s41467-023-41680-1

Levitas, V. I., Esfahani, S. E., & Ghamarian, I. (2018). Scale-free modeling of coupled evolution of discrete dislocation bands and multivariant martensitic microstructure. *Physical Review Letters*, *121*(20), 205701. https://doi.org/10.1103/physrevlett.121.205701

Levitas, V. I., Kamrani, M., & Feng, B. (2019). Tensorial stress-strain fields, large elastoplasticity, and friction in diamond anvil cell up to 400 GPa. *NPJ Computational Materials*, *5*(1), 94. https://doi.org/10.1038/s41524-019-0234-8

Levitas, V. I., & Shvedov, L. K. (2002). Low pressure phase transformation from Rhombohedral to cubic BN: Experiment and theory. *Physical Review B*, *65*(10), 104109. https://doi.org/10.1103/physrevb.65.104109

Li, J., & Hitch, M. (2016). Characterization of the microstructure of mechanically-activated olivine using X-ray diffraction pattern analysis. *Minerals Engineering*, *86*, 24–33. https://doi.org/10.1016/j.mineng.2015.11.010

Lutterotti, L., & Scardi, P. (1991). Profile fitting by the interference function. *Advances in X-Ray Analysis*, *35*(A), 577–584. https://doi.org/10.1154/s0376030800009277

Murr, L. E., & Kuhlmann-Wilsdorf, D. (1978). Experimental and theoretical observations on the relationship between dislocation cell size, dislocation density, residual hardness, peak pressure and pulse duration in shock-loaded nickel. *Acta Metallurgica*, *26*(5), 847–857. https://doi.org/10.1016/0001-6160(78)90034-2

Peng, Y., Ji, R., Phan, T., Capolungo, L., Levitas, V. I., & Xiong, L. (2023). Effect of a micro-scale dislocation pileup on the atomic-scale multi-variant phase transformation and twinning. *Computational Materials Science*, *230*, 112508. https://doi.org/10.1016/j.commatsci.2023.112508

Peng, Y., Ji, R., Phan, T., Gao, W., Levitas, V. I., & Xiong, L. (2022). An Atomistic-to-Microscale Computational Analysis of the dislocation pileup-induced local stresses near an interface in plastically deformed two-phase materials. *Acta Materialia*, *226*, 117663. https://doi.org/10.1016/j.actamat.2022.117663

Ribárik, G. (2008). *Modeling of diffraction patterns based on microstructural properties*. Eötvös Loránd University.

Ribárik, G., Ungár, T., & Gubicza, J. (2001). MWP-fit: A program for multiple whole-profile fitting of diffraction peak profiles by ab initio theoretical functions. *Journal of Applied Crystallography*, *34*(5), 669–676. https://doi.org/10.1107/s0021889801011451

Scardi, P. (2020). Diffraction line profiles in the Rietveld method. *Crystal Growth and Design*, *20*(10), 6903–6916. https://doi.org/10.1021/acs.cgd.0c00956

Scardi, P., & Leoni, M. (2004). Whole powder pattern modelling: Theory and applications. In *Diffraction analysis of the microstructure of materials* (pp. 51–91). Springer Berlin Heidelberg.

Scardi, P., Leoni, M., & Delhez, R. (2004). Line broadening analysis using integral breadth methods: A critical review. *Journal of Applied Crystallography*, *37*(3), 381–390. https://doi.org/10.1107/s0021889804004583

Ungár, T., & Borbély, A. (1996). The effect of dislocation contrast on X-ray line broadening: A new approach to line profile analysis. *Applied Physics Letters*, *69*(21), 3173–3175. https://doi.org/10.1063/1.117951

Voyiadjis, G. Z., & Yaghoobi, M. (2019). *Size Effects in Plasticity: From Macro to Nano*. Academic Press.

Supporting Information for

# Severe Strain-induced Olivine-Ringwoodite Transformation at Room Temperature: Key to Enigmas of Deep-Focus Earthquake

**F. Lin[1*], V. I. Levitas[1,2,3*], S. Yesudhas[1], A. Dhar[1], and J. Smith[4]**

[1]Department of Aerospace Engineering, Iowa State University, Ames, Iowa 50011, USA.

[2]Department of Mechanical Engineering, Iowa State University, Ames, Iowa 50011,USA.

[3]Ames National Laboratory, US Department of Energy, Iowa State University, Ames, Iowa 50011, USA.

[4]HPCAT, X-ray Science Division, Argonne National Laboratory, Argonne, Illinois 60439, USA.

## Contents

**Text S1. Estimation of dislocation density, crystallite size, and microstrain**

There are numerous methods for determining the crystallite size *d*, microstrain $\varepsilon_m$, and dislocation density $\rho$ from XRD based on different models and assumptions. Even for microstrains only, various techniques (e.g., analyzed in Li & Hitch, 2016 for olivine) give differences almost by an order of magnitude. It is even more complex for dislocation density, where additional assumptions are involved. That is why many advanced papers use a simple equation $\rho = K/d^2$ , where *K* is the constant proportionality factor. Factor $K$ varies from 1 to 100 (Lee at al., 2014) and even 225 (Murr & Kuhlmann-Wilsdorf, 1978) depending on the method, model, and whether dislocations in the cell walls are included or not. *However, the key point for all approaches is that since they are consistently used for the entire data set, the relative variation of the crystallite size, microstrain, and dislocation density for different data points is consistent, and the evolution trend is valid and independent of the method used. Since all raw data are available, everyone will be able to recalculate the structural parameters using their own model.*

As an example, all line profile analysis (LPA) methods (Ribárik et al., 2001; Scardi et al., 2004) basically utilize the diffraction peak broadening and line shape for extraction of crystallite size and microstrain components. They are then employed to estimate microstructural parameters like dislocation density, stacking fault, twin probabilities, etc., based on various analytical models of their contributions to diffraction peak profiles (Ribárik, 2008). Generally, these analysis methods are used for materials with non-overlapping diffraction peaks, which is not the case here (Fig. 2). Any LPA method relies on the truncation of diffraction peak profiles in a finite range which poses serious limitations to reliable estimation of microstructural parameters, especially in cases of overlapping peaks. Another issue with the LPA method for our studies is the heterogenous macrostress states in RDAC along the sample thickness within the x-ray beam, which also contribute to the peak broadening and peak profile asymmetry. LPA methods utilize individual contrast factors of diffraction peaks as a scaling factor to include the strain anisotropy (Ungár & Borbély, 1996; Borbély & Ungár, 2012). However, reliable estimation of contrast factors for given strain anisotropy is a challenging task and a research problem in itself.

Presently, the whole powder pattern modeling methods based on the Rietveld refinement incorporating microstructural parameters, texture, stress heterogeneity, etc. (Lutterotti & Scardi, 1991; Scardi, 2020; Scardi & Leoni, 2004) provide more reliable estimates of microstrain and crystallite size. That is why this method, using MAUD software (Lutterotti et al., 1997), has been implemented in our study. The obtained microstrain and crystallite size have been further used to estimate the dislocation density with the widely used Williamson-Hall method (Williamson & Smallman, 1956).

Thus, the dislocation density can be expressed as:

$$\rho = \sqrt{\rho_c \rho_{ms}}\,. \tag{S1}$$

Here $\rho_c$ and $\rho_{ms}$ contribute to overall dislocation density from crystallite size and microstrain, respectively. Contribution from crystallite size is:

$$\rho_c = \frac{3n}{d^2}\,. \tag{S2}$$

Here *n* is the number of dislocations per block face. For severely deformed materials, in which dislocation distribution is nearly random within a grain, *n*=1 is a reasonable assumption

(Williamson & Smallman, 1956). Contribution from the microstrain is determined by the equation:

$$\rho_{ms} = k\varepsilon_m^2/b^2, \tag{S3}$$

where $b$ is the magnitude of the Burgers vector; $k = 6\pi A(\frac{E}{G\ln(r/r_0)})$ is a material constant; $E$ and $G$ are Young's modulus and shear modulus, respectively; $A$ is a constant that lies between 2 and $\pi/2$ based on the distribution of strain; $r$ is the radius of crystallite with dislocation; $r_0$ is a chosen integration limit for dislocation core. In this study, $A = \pi/2$ for the Gaussian distribution of strain. Moduli $E$, $G$ and their pressure dependence for San Carlos olivine are taken from Liu et al. (2005). A reasonable value of $\ln(r/r_0)$ being 4 is used (Williamson & Smallman, 1956). Olivine has the easiest and dominant slip system of $(010)[001]$; thus, the length of the Burger vector [001] is used (Raterron et al., 2014).

**Text S2. FEA of the shear banding in a sample compressed and sheared in RDAC**

Unfortunately, we could not check the existence of the shear-phase transformation bands on the retrieved sample because of the complete reverse phase transformation. Also, the sample was pulverized during the unloading. We also could not perform quantitative finite element simulations for the olivine-spinel system because phase transformation kinetics and pressure-, plastic strain-, grain size-, and dislocation density-dependent yield strength of phases during severe plastic flow are unknown and should be determined via coupled experimental-computational procedure (Dhar et al., 2024; Levitas et al., 2019; Levitas et al., 2023), which will be done in future. However, this was never done for a sample with shear bands, which significantly complicates the problem.

Under the circumstances, our goal here is to prove the existence of the phase transformation -shear band and reproduce the main unusual features of our experiments, namely incomplete phase transformation and oscillating character of the volume fraction of high-pressure phase $\bar{c}$ averaged over the sample thickness. It is known that shear banding occurs when material softens (i.e., the yield strength $\sigma_y$ reduces). For olivine, softening occurs because of phase transformation to ultrafine-grained ringwoodite (12-20 nm), with the yield strength of ~ 1 GPa, much lower than ~4.5 GPa for olivine (Mohiuddin et al., 2020). While in Mohiuddin et al. (2020), the yield strength of ringwoodite increased to ~ 3 GPa after 2.5 hours due to grain growth at 1173 K, there is no increase in the crystallite size in our room temperature experiment. The same transformational softening is expected for any material with the yield strength $\sigma_{y2}$ of the high-pressure phase much lower than that of the low-pressure phase $\sigma_{y1}$, independent of the elastic properties and specific phase transformation kinetics. That is why we will use a model with generic elastic properties, strain-controlled kinetics, and similar equations, properties, and problem formulation like in Feng and Levitas (2016) to simulate phase transformation -deformation processes in compression and torsion in RDAC. To be safe, the ratio $\sigma_{y2}/\sigma_{y1}$ is taken to be 0.3. Note that microstructural parameters do not participate in the simulations.

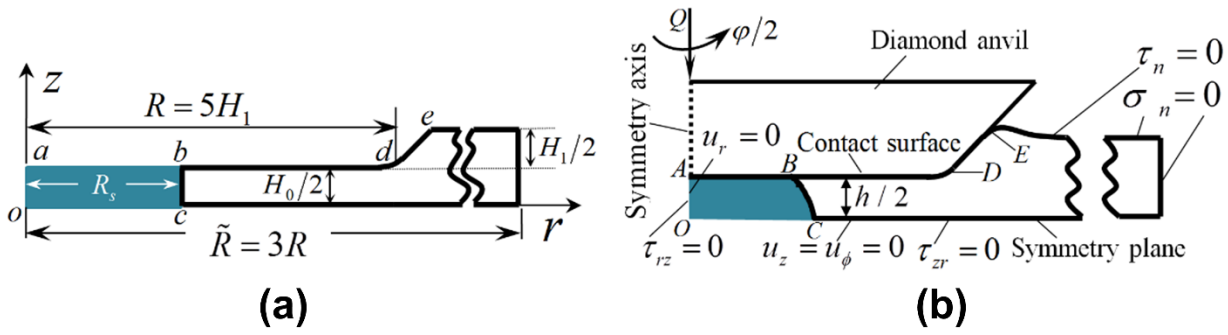


**Fig. S1 Geometry and boundary conditions.** (a) Scheme of the quarter of a sample and gasket in RDAC in the initial undeformed state; (b) geometry of a sample and gasket in RDAC in the deformed configuration and boundary conditions. In simulations, $R_s = 2H_0$ and $H_1 = H_0$.

The geometry of RDAC is shown in Fig. 1b. The geometry of the sample and the anvil, as well as the boundary conditions, are shown in Fig. S1. They are as follows:
(1) At the symmetry axis $r = 0$ (z-axis), $\tau_{rz}$ and radial displacement are zero. At the symmetry plane $z = 0$, shear stress $\tau_{rz}$ and axial and circumferential displacements are zero.
(2) At the contact surface between the sample and the anvil, an isotropic friction model, described in Feng and Levitas (2016), is utilized. Due to the high friction coefficient $\mu$ =0.3 and high pressure in the sample, there is cohesion between the sample and anvil. After shear stress reaches the yield strength in shear, localized shear occurs in a thin contact layer, producing a shear- phase transformation band (Fig. 3F).

(3) Other surfaces not mentioned above are stress-free.
Diamonds are considered to be rigid and vertical force and rotation angle are applied to the upper diamond.
Obtained solution is presented and analyzed in the main text.

**Text S3. Experimental relationships between the minimum phase transformation pressure, microstructural parameters, and plastic strain**

Data in Fig. 4 are obtained as follows. For each shear, the precise material position corresponding to the initiation of phase transformation ($\bar{c} = 0$) lies between two adjacent diffraction data points, one with no PT detected and the other with a tiny amount of ringwoodite. The values of minimum pressure for strain-induced phase transformation $p_\varepsilon^d$ and corresponding plastic strain $q$ are the average of these two points with error bars covering the range between. For better statistical representation, the values of corresponding microstructural parameters in Fig. 4 are averaged over a few data points around the edge with $\bar{c} \in [0, 0.1]$, and the error bar is the standard deviation for these points.

The minimum phase transformation pressure can be approximately described by a linear function of the plastic strain within the experimental range (Fig. 4a):

$$p_\varepsilon^d(GPa) = -1.31(\pm 0.23)q + 27.01(\pm 1.63); \qquad q \text{ is the accumulated plastic strain.} \quad \text{(S4)}$$

Similarly, the minimum PT pressure can be approximately described by a linear function of the microstructural parameters (Fig. 4b-d):

$$p_{\varepsilon}^{d}(GPa) = 1.13(\pm 0.16)d_{ol} - 4.68(\pm 3.22); \quad \text{(S5)}$$

$$p_{\varepsilon}^{d}(GPa) = -2.95(\pm 1.13)\varepsilon_m + 49.17(\pm 11.92); \quad \text{(S6)}$$

$$p_{\varepsilon}^{d}(GPa) = -2.04(\pm 0.23)\rho_{ol} + 32.52(\pm 1.61). \quad \text{(S7)}$$

Since microstructural parameters are modified by plastic straining, the linear approximations for microstructural parameters versus plastic strain were obtained as well:

$$d = -0.68(\pm 0.40)q + 26.47(\pm 2.80); \quad d \text{ is the crystallite size of olivine in } (nm); \quad \text{(S8)}$$

$$\varepsilon_m = 0.41(\pm 0.08)q + 7.72(\pm 0.55); \quad \varepsilon_m \text{ is the microstrain of olivine in } (10^{-3}); \quad \text{(S9)}$$

$$\rho = 0.64(\pm 0.04)q + 2.66(\pm 0.30); \quad \rho \text{ is dislocation density in olivine in } (10^{14} m^{-2}). \quad \text{(S10)}$$

The advantage of Eq. (S5)-(S7) is that all involved parameters can be measured using XRD without evaluating the $q$. They can be obtained experimentally directly without involving Eq. (S8)-(S10).

One of the seeming contradictions is that the crystallite size, dislocation density, and microstrain in olivine reach steady values in Fig. 3c-e, but we found a reduction in phase transformation pressure with the decrease in the crystallite size and growth in dislocation density and microstrain in Fig. 4b-d. However, the steady state is claimed for the averaged values for all data in the statistical sense. At the same time, nucleation is determined by the strongest stress concentrator. For points corresponding to initiation of phase transformation, crystallite size reduces from 22 to 17 nm, dislocation density increases from 5.5 to $8.5\times10^{14}$ $m^{-2}$, and microstrain increases from 0.0095 to 0.0114 during the rotation angle increment from 270º to 330º.

**Text S4. Comments on dislocation pileup-based mechanism of strain-induced phase transformations**

Severe plastic straining can drastically reduce the minimum phase transformation pressure for various material systems (Levitas, 2019; 2023). The largest known reduction is from 70 GPa under hydrostatic conditions to 0.7 GPa under shear in RDAC for graphite to cubic diamond phase transformation (Gao et al., 2019). Phase transformation pressure in 100 nm Si particles for transformation from Si-I to Si-II was reduced from 16.2 GPa in He pressure transmitting medium to 0.3 GPa under plastic straining (Yesudhas et al., 2024). For phase transformation from hexagonal to wurtzitic BN, reduction in phase transformation pressure is from 52 GPa to 6.7 GPa (Ji et al., 2012), and from 55 GPa to 5.6 GPa for rhombohedral to cubic BN (Levitas & Shvedov, 2002). Under hydrostatic conditions and room temperature, olivine does not transform to spinel at all; in this study, olivine is transformed to ringwoodite in RDAC at 15 GPa. The only known mechanism that can explain such a drastic reduction in the minimum phase transformation pressure for strain-induced transformation is the nucleation at the dislocation pileup. It was suggested and justified analytically in Levitas (2004) with the nanoscale (Javanbakht & Levitas, 2016; Levitas & Javanbakht, 2014) and microscale (Levitas et al., 2018) phase field approach, molecular dynamics (Chen et al., 2019), and concurrent atomistic-continuum simulations (Peng et al., 2022; 2023) for over last 20 years. The pressure-

and stress-induced phase transformations start with nucleation at the pre-existing defects. Conversely, the plastic strain-induced phase transformations start at new defects, like dislocation pileups, continuously generated during the plastic flow. Strong concentration of all components of the stresses tensor $\boldsymbol{\sigma}$ at the tip of dislocation pileup is proportional to the number of dislocations $N$ in a pileup, which can be 10 and even 100. Also, the shear stresses in a small nanoscale region near the tip of the dislocation pileup are limited by the theoretical shear strength, which can be 2 to 3 orders of magnitude larger than the macroscopic yield strength. Such huge local highly nonhydrostatic stresses reach the limit of the crystal lattice instability and lead to barrier nucleation of the high-pressure phase on the sub-nanosecond time scale at the external pressure much lower than under hydrostatic conditions.

Kinetic equation (1) was derived in Levitas (2004) based on this mechanism and confirmed quantitatively for α-ω transformation in Zr (Pandey & Levitas, 2020, Dhar et al., 2024). Strong experimental confirmation of the predictions based on the dislocation pileup-based mechanism was obtained for phase transformations in Si (Yesudhas et al., 2024):

(a) Theoretically predicted correlation between the grain size dependence of the phase transformation pressure for strain-induced phase transformation and direct and inverse Hall-Petch relationships for yield strength was confirmed experimentally.

(b) Pressure in small Si-II regions is ~5-7 GPa higher than in Si-I for micron and 100 nm Si, while for pressure-induced phase transformation, it is by 2.7 GPa lower due to 22% volume reduction, clearly showing strong stress concentration. For 30 nm Si, the difference is 1.6 GPa only, consistent with reduced dislocation activity in the region of the inverse Hall-Petch effect and increased phase transformation pressure. A similar difference in pressure in Si-I and Si-III is observed in 100 nm Si. Such a strong stress concentrator could be produced by the dislocation pileups only.

The goal of this paper is not to revisit this mechanism since we did not get any data that contradict it. We are just discussing some results in terms of only known mechanism. This is not mandatory for the main goal of the paper but supposed to be useful and refreshing to the geophysics topic.

Thus, it follows from the results of the phase field (Javanbakht & Levitas, 2016; Levitas & Javanbakht, 2014) and atomistic simulations (Chen et al., 2019, Peng et al., 2022; Peng et al., 2023) that almost all dislocations are concentrated at the grain boundary, producing a superdislocation or step (Fig. S2). All components of the stress tensor $\boldsymbol{\sigma}$ field of an edge superdislocation are $\boldsymbol{\sigma}\sim\mu Nb/r$ (Anderson et al., 2017), where $\mu$ is the shear modulus, $N$ is the number of dislocations in a pileup, $b$ is the magnitude of the Burgers vector, and $r$ is the distance from the superdislocation. Since $N$ can be from 10 to 100, local stresses are greatly multiplied, drastically reducing the external pressure $p$ required for phase transformation. The number of dislocations equilibrated in a superdislocation $N\sim\tau^{\alpha} = \tau_y^{\alpha}$ (Peng et al., 2022; Peng et al., 2023), where α is the exponent. Combining the above equations, we obtain $\boldsymbol{\sigma}\sim\mu\tau_y^{\alpha}b/r$. Then, combining the Hall-Petch contribution due to grain size $d$ and the Taylor contribution due to dislocation density $\rho$ (Voyiadjis et al., 2019), one obtains:

$$\tau_y = \tau_0 + kd^{-0.5} + m\rho^{0.5}, \tag{S11}$$

where $\tau_0$, $m$, and $k$ are material parameters. That explains why $\tau_y$ and stress concentration increases, and the minimum pressure for the strain-induced phase transformation decreases with decreasing grain size and increasing dislocation density (Fig. 4b, c). Also, the higher $\rho$ is, the higher the probability of generating more dislocation pileups with large $N$. Lowering $d$: (a) reduces chances for dislocation forest, increasing the probability of dislocation pileups, and (b)

increases misorientation between grains, increasing resistance for dislocations to pass through the grain boundary. Plastic straining is the means for increasing the dislocation density, reducing the crystallite size, and bringing up more dislocation pileups with larger *N* for stronger stress concentrators.

Small crystallite size after strain-induced phase transformation was predicted for nucleation at the tip of the dislocation pileup (Levitas, 2004) because all stresses reduce fast (as *1/r*) away from the tip, and crystallite growth is inhibited. The crystallite size of ringwoodite essentially does not change with increasing $\bar{c}$ (Fig. 3c, d), implying that ringwoodite keeps nucleating without further growth during the SPD.

Note that none of the microstructural parameters (crystallite size, dislocation density, and microstrain) can be directly related to the strong stress concentration at the tip of the dislocation pileup since they are averaged over the beam area and sample thickness. But dislocation density and crystallite size contribute to the yield strength through Eq. (S11), which participate in the description of stress concentrator at the tip of dislocation pileup $\sigma \sim \mu \tau_y^{\alpha} b/r$.

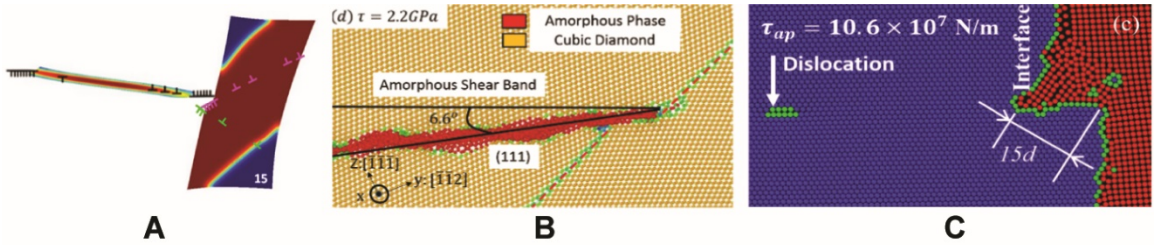


**Fig. S2. Dislocation pileups produce a step at the grain boundary or phase interface that causes a phase transformation.** (a) Dislocation pileup in the left grain produces a step at the grain boundary and cubic to tetragonal phase transformation and dislocation slip in the right grain. Phase-field approach results from Javanbakht and Levitas (2016). (b) Dislocation pileup in the right grain produces a step at the grain boundary in Si I and amorphization in the left grain. Molecular dynamics results from Chen et al. (2019). (c) Step at the phase interface boundary consisting of 15 dislocations and causing cubic to hexagonal phase transformation. The atomistic portion of the concurrent continuum-atomistic approach is from Peng et al. (2023). Adopted with changes from Javanbakht and Levitas (2016); Chen et al. (2019); Peng et al. (2023) with permissions.

**Text S5. Summary of the suggested mechanochemical mechanism of the deep-focus earthquake (Levitas, 2022)**

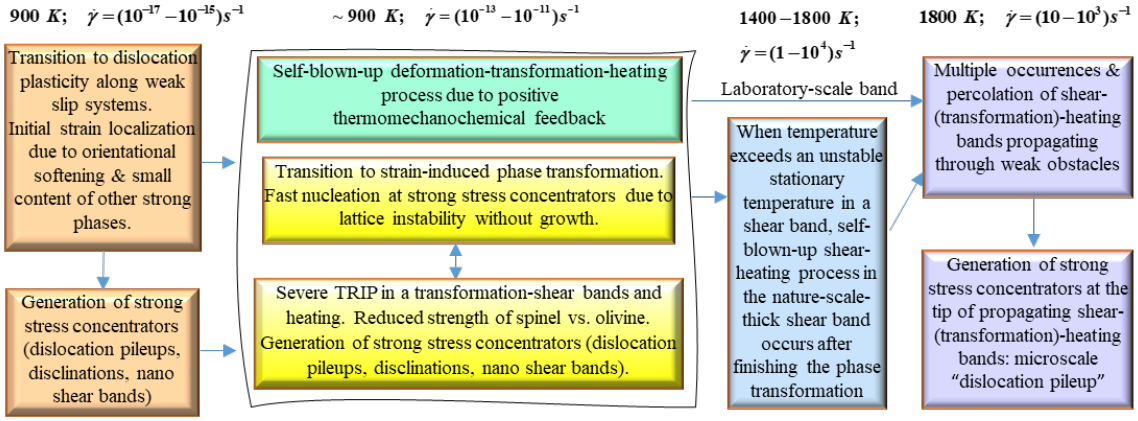


**Fig. S3. Schematics of the mechanisms of localized thermoviscoplastic flow and phase transformation leading to high strain and phase transformation rates and temperatures in phase transformation -deformation bands.** Temperature and shear rate before each stage are shown on the top (adopted from Levitas, 2022).

To outline the relationship between the current experimental results and the theoretical mechanism of the deep-focus earthquake suggested and quantitatively justified in Levitas (2022), we summarize the main point of the mechanism. They are schematically presented in Fig. S3, which contains several conceptually important points.

1. Proof that thermoplastic flow alone cannot localize in a mm-scale band and cause strong heating; that is why phase transformation is required.
2. Initial strain localization occurs due to transition from diffusional creep to dislocation glide along properly oriented weak [001](010) slip systems and related orientational softening, as well as along the path with a minor content of other strong phases, like diopside or garnet.
3. Localized plastic flow leads to the generation of dislocation pileups, producing strong concentrators of all components of the stress tensor.
4. Dislocation pileups lead to the substitution of stress/pressure-induced phase transformation with plastic strain-induced phase transformation, which has an entirely different kinetic equation. The phase transformation rate is proportional to the strain rate, which explains a high transformation rate for high strain rates.
5. Volume reduction during phase transformation in a shear band generates severe transformation-induced plasticity (TRIP) and heating, which soften the material and increase strain rate, leads to faster strain-induced phase transformation. This in turn causes faster TRIP (i.e., higher strain rate) and heating, and so on, i.e., self-blown-up phase transformation -TRIP heating process. Strain-induced phase transformation, TRIP, and heating form a mutual promotion loop resulting in the self-blown-up phase transformation -TRIP-heating process due to positive thermomechanochemical feedback. This process leads to completing the phase transformation within a few seconds. Severe TRIP shear also accounts for the shear-dominated seismic signals from the DFE. The current experiment proves that even without heating, phase transformation can be completed within tens of seconds. Current simulations show that phase transformation to the weaker high-pressure phase leads to the formation of the shear transformation bands.

6. The self-blown-up phase transformation -TRIP leads to the heating above the unstable stationary temperature in the range of 1400-1800 K, after which further heating in a shear band occurs due to traditional thermoplastic flow, and the shear band can propagate through other non-transforming phases. Heating to 1800 K is enough to get a strain rate of 10-$10^3$/s and generate strong seismic waves. However, in the laboratory, due to very thin shear- phase transformation bands, heating does not occur, and shear strain due to the self-blown-up phase transformation -TRIP process is orders of magnitude smaller than in nature.
7. Similar processes occur in multiple phase transformation-shear bands and, after completing phase transformation, only shear bands that find paths through weak obstacles. They may percolate and magnify generated seismic waves. These bands produce strong stress concentrators at their tips and represent a larger scale counterpart of a dislocation pileup, which causes both fast phase transformation and plasticity and further propagation of a shear band, through repeating the above processes at a larger scale.

The current paper does not aim to discuss, modify, or further develop this mechanism. We focus on experimental justification of the strain-induced character of olivine-ringwoodite phase transformation only (point 4), which is crucial for all the following processes (points 5 to 7).

**Text S6. Notes on the temperature increase during plastic flow and its possible effect on olivine-ringwoodite phase transformation**

One of the attempts to explain the effect of the plastic shear on phase transformations is that it generates large local heating, which accelerates the phase transformation kinetics. However, it is an unrealistic assumption. First, heating in the dRDAC is negligible due to the high thermal conductivity of diamonds (2.2 KW/(m·K)) and the very thin sample. We used a rotation speed of 0.1 RPM and no rotations for XRD measurements after each step. A significant part of phase transformation occurred at 30º rotation increment between $\phi$=270º and 300º (which takes 50 s) (Fig. 3b). Even for large-scale high-pressure torsion with steel anvils (with thermal conductivity of just 40 W/(m·K)), 16 times thicker Mo sample, the rotation speed of 1 RPM, and after 50 s, increase in temperature was ~40 K. Therefore, after 5 s, which gives the same rotation of 30º like in our experiment, the temperature increase is negligible (Edalati et al., 2011). Even if we assume significant local heating (to 850-1000 K), this will not help with phase transformation. Indeed, in nonhydrostatic DAC experiments on $Mg_2SiO_4$ (Wu et al., 1993), the thin β-spinel film appeared at the diamond surface at 19-35 GPa after holding at 575ºC for 10.5 hours. No phase transformation was found in bulk, which indicates that this phase transformation is induced by large plastic shears due to the friction in the contact region. Even at 28-32 GPa and heating to 650ºC for 8 hours, only wadsleyite was observed in bulk without ringwoodite. Also, in experiments involving plastic deformation of olivine (Mohiuddin et al., 2020; Ohuchi et al., 2022), heating above 1100 K for hours is required for phase transformation to occur.

Thus, heating cannot be the reason for phase transformation. This is also clear from the phase transformations in other materials, in which phase transformation occurs deeply in the region of stability of the low-pressure phase. For example, phase equilibrium pressure for Si-I and Si-II phases is 10-12 GPa, and it is weakly dependent on temperature. Under plastic deformations, Si-I→Si-II phase transformation was recorded at 0.3 GPa (Yesudhas et al., 2024), while temperature should promote the reverse phase transformation in this case.

**Text S7. Some opportunities with rough diamond anvils (rough-DA)**

In high-pressure torsion processing with metallic/ceramic anvils, which is used for producing nanostructured materials (Edalati et al., 2022), friction reaches the maximum possible level due to large asperities. Due to the low friction coefficient of the diamond, there is significant relative sliding between the smooth anvil culet and the sample, which significantly lowers the shear strain imposed and leads to an indeterminacy in the boundary condition for modeling the deformation of the sample. Utilizing dRDAC with rough-DA will enable in-situ study of high-pressure SPD and optimization of occurring processes. Also, an increase in friction with rough-DA not only intensifies plastic flow but also increases pressure gradient, which increases the maximum possible pressure achieved in the DAC and RDAC.

**Table S1.** Composition of the San Carlos olivine in this study.

| | **O** | **Mg** | **Si** | **Ca** | **Cr** | **Mn** | **Fe** | **Ni** |
|---|---|---|---|---|---|---|---|---|
| **Atom (%)** | 56.31 | 26.53 | 14.41 | 0.03 | 0.01 | 0.04 | 2.57 | 0.11 |
| **Weight (%)** | 42.81 | 30.65 | 19.24 | 0.05 | 0.03 | 0.10 | 6.82 | 0.31 |

**Table S2.** Compression-shear steps in the experiment and the corresponding sample thickness

| **Step** | **Initial** | **Compression before 60º shear** | **After 60º shear** | **Compression before 180º shear** | **After 180º shear** |
|---|---|---|---|---|---|
| **Thickness (μm)** | 149 | 104 | 75 | 73 | 53 |
| **Step** | **Compression before 270º shear** | **After 270º shear** | **After 300º shear** | **After 330º shear** | |
| **Thickness (μm)** | 48 | 44 | 40 | 34 | |

**References**


1. Anderson, P.M., Hirth, J.P. & Lothe, J. Theory of dislocations. Cambridge University Press, (2017).
2. Borbély, A. & Ungár, T. X-ray line profiles analysis of plastically deformed metals. *Comptes Rendus Physique*, 13(3), 293-306 (2012).
3. Chen, H., Levitas, V.I. & Xiong, L. Amorphization induced by 60° shuffle dislocation pileup against different grain boundaries in silicon bicrystal under shear. *Acta Materialia*, 179, 287-295 (2019).
4. Dhar, A., Levitas, V.I., Pandey, K.K., Park, C., Somayazulu, M. & Velisavljevic, N. Quantitative kinetic rules for plastic strain-induced α-ω phase transformation in Zr under high pressure. Npj Computational Materials,10, 290 (2024).
5. Edalati, K., Bachmaier, A., Beloshenko, V.A. et al. Nanomaterials by severe plastic deformation: Review of historical developments and recent advances. *Materials Research Letters*, 10(4), 163-256 (2022).
6. Edalati, K., Miresmaeili, R., Horita, Z., Kanayama, H. & Pippan, R. Significance of temperature increase in processing by high-pressure torsion. *Materials Science and Engineering A*, 528, 7301-7305 (2011).
7. Feng, B. & Levitas, V.I. Effects of gasket on coupled plastic flow and strain-induced phase transformations under high pressure and large torsion in a rotational diamond anvil cell. *Journal of Applied Physics*, 119, 015902 (2016).
8. Gao, Y., Ma, Y., An, Q., Levitas, V.I., Zhang, Y., Feng, B., Chaudhuri, J. & Goddard III, W.A. Shear driven formation of nano-diamonds at sub-gigapascals and 300 K. *Carbon*, 146, 364-368 (2019).
9. Javanbakht, M. & Levitas, V.I. Phase field simulations of plastic strain-induced phase transformations under high pressure and large shear. *Physical Review B*, 94(21), 214104 (2016)
10. Ji, C., Levitas, V.I., Zhu, H., Chaudhuri, J., Marathe, A. & Ma, Y. Shear-Induced Phase Transition of Nanocrystalline Hexagonal Boron Nitride to Wurtzitic Structure at Room Temperature and Low Pressure. *Proceedings of the National Academy of Sciences of the USA*, 109, 19108-19112 (2012).
11. Lee, D.J., Yoon, E.Y., Ahn, D.H., Park, B.H., Park, H.W., Park, L.J., Estrin, Y. & Kim, H.S. Dislocation density-based finite element analysis of large strain deformation behavior of copper under high-pressure torsion. *Acta Materialia*, 76, 281-293 (2014).
12. Levitas, V.I. High-Pressure Mechanochemistry: Conceptual Multiscale Theory and Interpretation of Experiments. Physical Review B, 70(18), 184118 (2004).
13. Levitas, V.I. High-Pressure Phase Transformations under Severe Plastic Deformation by Torsion in Rotational Anvils. *Material Transactions*, 60, 1294-1301 (2019).
14. Levitas V.I. Resolving puzzles of the phase-transformation-based mechanism of the deep-focus earthquake. *Nature Communications*, 13(1), 6291 (2022).
15. Levitas V.I. Recent in situ Experimental and Theoretical Advances in Severe Plastic Deformations, Strain-Induced Phase Transformations, and Microstructure Evolution under High Pressure. *Material Transactions*, 64, 1866-1878 (2023).
16. Levitas, V.I., Dhar, A. & Pandey K.K. Tensorial stress-plastic strain fields in alpha-omega Zr mixture, transformation kinetics, and friction in diamond anvil cell. *Nature Communications*, 14, 5955 (2023).

17. Levitas, V.I., Esfahani, S.E. & Ghamarian, I. Scale-free modeling of coupled evolution of discrete dislocation bands and multivariant martensitic microstructure. *Physical review letters*, 121(20), 205701 (2018).
18. Levitas, V.I. & Javanbakht, M. Phase transformations in nanograin materials under high pressure and plastic shear: nanoscale mechanisms. *Nanoscale*, 6(1), 162-166 (2014).
19. Levitas, V.I., Kamrani, M. & Feng, B. Tensorial stress-strain fields, large elastoplasticity, and friction in diamond anvil cell up to 400 GPa. *NPJ Computational Materials*, 5, 94 (2019).
20. Levitas, V.I. & Shvedov, L.K. Low Pressure Phase Transformation from Rhombohedral to Cubic BN: Experiment and Theory. *Physical Review B*, 65(10), 104109 (2002).
21. Li, J. & Hitch, M. Characterization of the microstructure of mechanically-activated olivine using X-ray diffraction pattern analysis. *Minerals Engineering*, 86, 24-33 (2016).
22. Liu, W., Kung, J. & Li, B. Elasticity of San Carlos olivine to 8 GPa and 1073 K. *Geophysical Research Letters*, 32(16) (2005).
23. Lutterotti, L., Matthies, S., Wenk., H.R., Schultz, A.S. & Richardson Jr, J.W. Combined texture and structure analysis of deformed limestone from time-of-flight neutron diffraction spectra. *Journal of Applied Physics*, 81, 594-600 (1997).
24. Lutterotti, L. & Scardi, P. Profile fitting by the interference function. *Advances in X-ray Analysis*, 35(A), 577-584 (1991).
25. Murr, L.E. & Kuhlmann-Wilsdorf, D. Experimental and theoretical observations on the relationship between dislocation cell size, dislocation density, residual hardness, peak pressure and pulse duration in shock-loaded nickel. *Acta Metallurgica*, 26(5), 847-857 (1978).
26. Mohiuddin, A., Karato, S.-I. & Girard, J. Slab weakening during the olivine to ringwoodite transition in the mantle. Nature Geoscience, 13, 170-174 (2020).
27. Ohuchi, T., Higo, Y., Tange, Y., Sakai, T., Matsuda, K. & Irifune, T. In situ X-ray and acoustic observations of deep seismic faulting upon phase transitions in olivine. *Nature Communication*, 13, 5213 (2022).
28. Pandey, K.K. & Levitas, V.I. In situ quantitative study of plastic strain-induced phase transformations under high pressure: Example for ultra-pure Zr. Acta Materialia, 196, 338-346 (2020).
29. Peng, Y., Ji, R., Phan, T., Capolungo, L., Levitas, V.I. & Xiong, L. Effect of a micro-scale dislocation pileup on the atomic-scale multi-variant phase transformation and twinning. *Computational Materials Science* 230, 112508 (2023).
30. Peng, Y., Ji, R., Phan, T., Gao, W., Levitas, V.I. & Xiong, L. An Atomistic-to-Microscale Computational Analysis of the dislocation pileup-induced local stresses near an interface in plastically deformed two-phase materials. *Acta Materialia*, 226, 117663 (2022).
31. Raterron, P., Detrez, F., Castelnau, O., Bollinger, C., Cordier, P. & Merkel, S. Multiscale modeling of upper mantle plasticity: from single-crystal rheology to multiphase aggregate deformation. *Physics of the Earth and Planetary Interiors*, 228, 232-243 (2014).
32. Ribárik, G. Modeling of diffraction patterns based on microstructural properties. *Eötvös Loránd University* (2008).
33. Ribárik, G., Ungár, T. & Gubicza, J. MWP-fit: a program for multiple whole-profile fitting of diffraction peak profiles by ab initio theoretical functions. *Journal of applied crystallography*, 34(5), 669-676 (2001).
34. Scardi, P. Diffraction line profiles in the Rietveld method. *Crystal Growth & Design*, 20(10), 6903-6916 (2020).

35. Scardi, P. & Leoni, M. Whole powder pattern modelling: Theory and applications. In *Diffraction analysis of the microstructure of materials* (pp. 51-91). Berlin, Heidelberg: Springer Berlin Heidelberg (2004).
36. Scardi, P., Leoni, M. & Delhez, R. Line broadening analysis using integral breadth methods: a critical review. *Journal of Applied Crystallography*, 37(3), 381-390 (2004).
37. Ungár, T. & Borbély, A. The effect of dislocation contrast on x-ray line broadening: A new approach to line profile analysis. *Applied Physics Letters*, 69(21), 3173-3175 (1996).
38. Voyiadjis, G.Z. & Yaghoobi, M. Size effects in plasticity: from macro to nano. Academic Press, (2019).
39. Williamson, G.K. & Smallman, R.E. III. Dislocation densities in some annealed and cold-worked metals from measurements on the X-ray Debye-Scherrer spectrum. *Philosophical Magazine*, 1, 34-46 (1956).
40. Wu, T.C., Bassett, W.A., Burnley, P.C. & Weathers, M.S. Shear-promoted phase transitions in $Fe_2SiO_4$ and $Mg_2SiO_4$ and the mechanism of deep earthquakes. *Journal of Geophysical Research: Solid Earth*, 98 (B11), 19767-19776 (1993).
41. Yesudhas, S., Levitas, V.I., Lin, F., Pandey, K.K. & Smith, J. Unexpected plastic strain-induced phase transformation phenomena in silicon. Nature Communications, 15, 7054 (2024).